The Astrophysical Journal Supplement Series, 270:2 (16pp), 2024 January https://doi.org/10.3847/1538-4365/ad0379

Experimental Phase Function and Degree of Linear Polarization of Light Scattered by Hydrogenated Amorphous Carbon Circumstellar Dust Analogs

Juan Carlos Gómez Martín[1], Olga Muñoz[1], Julia Martikainen[1], Daniel Guirado[1], Isabel Tanarro[2], Ramón J. Peláez[2], Belén Maté[2], Miguel Jiménez-Redondo[2,4], Víctor J. Herrero[2], Marco Peiteado[3], and Teresa Jardiel[3]
[1] Instituto de Astrofísica de Andalucía (IAA-CSIC), Glorieta de la Astronomía s/n, E-18008 Granada, Spain; jcgomez@iaa.es, olga@iaa.es
[2] Instituto de Estructura de la Materia (IEM-CSIC), Serrano 121–123, E-28006 Madrid, Spain
[3] Instituto de Cerámica y Vidrio (ICV-CSIC), Kelsen 5, Campus Cantoblanco, E-28049 Madrid, Spain
Received 2023 April 20; revised 2023 September 25; accepted 2023 October 13; published 2023 December 12

Abstract

Astronomical observations of the polarized intensity of scattered visible light have revealed the presence of dust envelopes around different types of evolved stars. These observations have helped determine the diameter and width of dust shells around stars with unprecedented accuracy. Simple geometric particle models are used in order to retrieve dust properties from these observations. In this work, we have synthesized and characterized a particulate sample of hydrogenated amorphous carbon (HAC), which is considered to be a realistic carbonaceous interstellar dust analog based on infrared absorption spectroscopy, and we have measured its phase function and degree of linear polarization curves at 514 nm using the CODULAB apparatus at IAA-CSIC. The experimental light-scattering data has been examined in order to explore possible improvements in the interpretation of astronomical observations of circumstellar dust from the point of view of the retrieval of dust properties, including size and porosity. Our results suggest that circumstellar dust observations of linearly polarized scattered light, which are commonly attributed to a population of spherical grains with a radius of $\sim$0.1 μm, are consistent with larger porous aggregates composed of nanometer-sized grains. In addition, an internal 50wt% mixture of HAC and ultrafine forsterite powder has been generated to study the effect of the mixing of these two components on the light-scattering behavior of dust in cometary environments and protoplanetary disks. In this case, the HAC component, which is not very absorbent, has a very small effect, and the mixture scatters light similarly to the forsterite sample.

Unified Astronomy Thesaurus concepts: Laboratory astrophysics (2004); Experimental data (2371); Dust physics (2229); Astrophysical dust processes (99); Interstellar dust (836); Interstellar scattering (854); Circumstellar dust (236); Optical constants (Dust) (2270); Dust shells (414)

1. Introduction

Evolved stars are an important source of interstellar dust. Stellar pulsations or large-scale convective motions propagate gas above the surface of asymptotic giant branch (AGB) stars, which condenses forming cool dust stellar shells. The particles are accelerated away by radiation pressure originating an outflow of materials (Bladh et al. 2019), which eventually contributes to the dust budget of the interstellar medium (ISM). For many years, AGB stars have been considered the main source of interstellar dust (Demyk 2012), although the current understanding is that their contribution is insufficient to explain the depletion of refractories observed in the ISM (Draine 2003; Zhukovska et al. 2018).

Astronomical observations of the spectral energy distribution (SED) in the infrared (IR) and of polarimetric properties of scattered visible light have revealed the presence of dust envelopes around different types of AGB and post-AGB stars (Gledhill 2005; Ramstedt et al. 2011). Well-defined detached dust layers have been observed around carbon-rich evolved stars (González Delgado et al. 2003; Olofsson et al. 2010; Ramstedt et al. 2011; Maercker et al. 2014; Lau et al. 2022). The IR emission from the circumstellar envelope of the carbon-rich post-AGB star HD 56126 has been modeled with a mixture of non-hydrogenated amorphous carbon (amC), hydrogenated amorphous carbon (HAC), and other compounds such as magnesium sulfide (MgS) and titanium carbide (TiC; Hony et al. 2003). An entirely different population of circumstellar grains is formed in the outflows of oxygen-rich AGB stars, which are often surrounded by clumps of dust (Min et al. 2013; Khouri et al. 2015; Ohnaka et al. 2016; Adam & Ohnaka 2019). The observations of polarized scattered intensity have helped determine the diameter and width of dust shells and the location of dust clumps around stars with unprecedented accuracy. Furthermore, modeling of these observations has provided some clues about the properties of the dust particles, i.e., size, structure, and composition (González Delgado et al. 2003; Hony et al. 2003; Ohnaka et al. 2016). An increasing number of high angular resolution visible polarimetric observations of circumstellar dusty envelopes are being obtained with the Very Large Telescope (VLT)/SPHERE-ZIMPOL instrument (Khouri et al. 2018; Adam & Ohnaka 2019; Khouri et al. 2020; Cannon et al. 2021).

In laboratory experiments, acetylene (C_2H_2) polymerization induced by a radio-frequency (RF) plasma has been shown to produce dusty deposits made of HAC (Maté et al. 2016; Jiménez-Redondo et al. 2019; Maté et al. 2019). HAC includes a wide group of disordered materials that consist of a mixture of aliphatic and aromatic structures and have different C/H

[4] Present address: Max-Planck-Institute for Extraterrestrial Physics, Gießenbachstraße 1, D-85748, Garching, Germany.

ratios. In materials science, HAC is often understood as a solid with a relatively high proportion of sp^3 carbon, while in astrophysics the term also includes aromatic-rich, H-poor material, sometimes referred to as amorphous carbon (e.g., soot, carbon black (CB)). A comparison of the IR absorption spectra of laboratory-synthesized HAC particles and of interstellar dust IR observations suggests that particles generated in acetylene plasmas are similar to the population of polyaromatic carbonaceous particles present in the diffuse ISM (Kovačević et al. 2005; Maté et al. 2019; Herrero et al. 2022). C_2H_2 is one of the most abundant molecules in the circumstellar envelopes where dust is formed (Fonfria et al. 2008). HAC is a likely condensate in H-rich and C-rich stellar outflows (Duley 1985; Hony et al. 2003; Santoro et al. 2020), with variable C/H ratio depending on the chemical makeup of the star and the radiation field to which the dust particles are exposed in the ISM (Herrero et al. 2022). In summary, HAC particles generated in the laboratory by C_2H_2 polymerization are considered a class of chemical analogs of carbonaceous interstellar dust, notwithstanding the different polymerization and transformation mechanisms in a laboratory plasma and in the cool envelopes of carbon stars under different pressure, temperature, and irradiation conditions. Similarly, iron and magnesium-containing silicate smokes formed in furnace reactors are considered analogs of circumstellar silicate grains (Rietmeijer & Karner 1999; Nuth et al. 2000) formed in the envelopes of oxygen-rich AGB stars. These silicate grains may develop subsequently organic coatings by condensation of polycyclic aromatic hydrocarbons and other organics on their surfaces in the ISM (Jones et al. 2013).

Gas-to-particle conversion processes result in the formation of nanometer-sized, nearly spherical monomers, which aggregate forming larger micron-sized fluffy structures, as shown by experiments mimicking gas condensation around oxygen-rich stars (Rietmeijer & Karner 1999; Nuth et al. 2000). For porous aggregates like these, the phase function (i.e., the angular dependence of the scattered light flux) is mainly determined by the size of the aggregate with an effective refractive index, while the degree of linear polarization (DLP) is determined by the size of the monomers (Gustafson & Kolokolova 1999; Hadamcik et al. 2006; Volten et al. 2007; Tazaki et al. 2016; Tazaki & Dominik 2022). However, circumstellar dust particles are usually modeled as distributions of spheres or hollow spheres to simplify calculations. In the context of imaging polarimetry of protoplanetary disks, it is known that these simple geometries are unable to reproduce simultaneously the phase angle dependence of the intensity and the DLP of the scattered light (Min et al. 2016; Arriaga et al. 2020). Furthermore, we have shown previously that modeling light scattering by irregular particles under the assumption of spherical symmetry leads to an overestimation of the imaginary part of the refractive index or an underestimation of particle size (Muñoz et al. 2021). A simple approach to mimic aggregate particles is the method of ballistic agglomeration (BA), although the calculation of the optical properties of aggregate dust particles by the discrete dipole approximation is still computationally time-consuming—if possible at all—for particles larger than the incident wavelength. In this context, laboratory studies of the light-scattering properties of realistic analogs may help in the interpretation of polarimetric astronomical observations and in the validation of models.

The light-scattering properties of silicate circumstellar dust analogs have been previously studied in the laboratory (Hadamcik et al. 2007; Volten et al. 2007). Carbon dust analogs (e.g., black carbon) were also mixed with silicate fluffy dust in order to investigate the influence of the carbon content on the scattering matrix (Hadamcik et al. 2006). However, the properties of carbon circumstellar dust analogs generated by relevant chemistry have not been studied experimentally. Here, we present measurements of the phase function and the DLP of HAC particle analogs generated by plasma deposition in an RF discharge and we compare these new measurements with previous experimental data for silicate circumstellar dust analogs also generated by gas-to-particle conversion. The scattering matrix of an internal mixture of amorphous carbon aggregates and submicron forsterite grains has also been measured. Such a mixture would not be directly relevant for the envelopes of aging stars with $C/O \sim 1$, where the silicate and carbonaceous fractions would both have in principle a similarly porous structure. However, particles composed of compact grains embedded in a porous matrix of smaller monomers have been identified as a morphological class of cometary dust particles (Güttler et al. 2019). Therefore, here we use our HAC material to generate samples where the effect of embedding silicate grains in the fluffy carbonaceous matrix can be studied.

2. Experimental Methods

2.1. Generation of HAC Dust Analogs

Carbon dust analogs were generated at the Cold Plasma Laboratory at the Instituto de Estructura de la Materia (IEE-CSIC). It consists of a highly instrumented low-pressure plasma reactor where analogs of cosmic dust grains are produced under controlled conditions and the gas-to-particle conversion processes can be analyzed in situ (Jiménez-Redondo et al. 2019). Moreover, several techniques are available to characterize the HAC samples ex situ, such as Fourier transform infrared (FTIR) spectroscopy, scanning electron microscopy (SEM), or UV-visible reflectivity measurements. The ultimate goal of this facility is to produce analogs of interstellar dust with the same spectroscopic features as those observed in ISM dust (Molpeceres et al. 2017), and to use these analogs for studies of energetic processing (Maté et al. 2016) and other processes like thermal desorption under ISM-relevant conditions (Maté et al. 2019).

HAC dust deposits were produced in this facility as described in previous publications (Maté et al. 2016; Jiménez-Redondo et al. 2019; Maté et al. 2019). Briefly, a capacitively coupled RF discharge (13.54 MHz, 15 W) on a gas mixture of acetylene (C_2H_2) and argon (2 sccm C_2H_2 + 5 sccm Ar, P = 0.31 mbar) triggers gas-phase ionic and neutral polymerization (Jiménez-Redondo et al. 2019, 2022). In the experiments carried out in the present work, the discharge had a duration of 80 minutes and was modulated with on/off cycles of 14 s/6 s. During the *on* part of the cycle, particles were formed and grew between the electrodes, and during the *off* part, they fell by gravity. Dust production can be diagnosed by 532 nm laser light scattering, recorded with a CCD camera, and it can also be directly followed by the naked eye with the aid of a broadband light source. In this setup, aluminum substrates are placed directly on top of the bottom electrode in order to collect dust deposits for ex situ spectroscopic analysis. A larger amount of sample required for scattering matrix measurements

was obtained by scrapping deposits from the stainless-steel inner surfaces of the reactor (including the electrode surfaces and the reactor walls) using a razor blade. The dust samples are light brown in color and tend to aggregate.

Besides the HAC circumstellar dust analog generated as indicated above, an additional sample was created by mixing a fraction of the HAC powder with forsterite fine powder (50wt% mixture). The forsterite sample was characterized elsewhere by X-ray diffraction and energy dispersive X-ray (EDX) spectroscopy (Muñoz et al. 2021). These analyses indicate an iron-poor forsterite composition with minor traces of other mineral phases. This sample has a narrow submicron-sized distribution labeled as XS to distinguish it from other narrow-sized fractions (*S*, *M*, and *L*) as described in detail by Muñoz et al. (2021).

2.2. Light-scattering Measurements

The Cosmic Dust laboratory at the Instituto de Astrofísica de Andalucía (IAA-CSIC) consists of a polar nephelometer, which has been described in detail elsewhere (Muñoz et al. 2010, 2011). Briefly, light from a diode laser (available wavelengths are 405, 488, 514, and 640 nm) passes through a polarizer and an electro-optic modulator before hitting a sample placed at the center of the setup. The light scattered by the sample is detected by two photomultipliers (detector and monitor). The detector moves along a ring spanning a range of scattering angles from $\theta = 3°$ to 177°, while the monitor is placed at a fixed angular position and tracks the fluctuations of the laser signal and/or dust jet stream from the aerosol generator. The polarization modulation of the incident light, in combination with additional polarimetric optical elements placed in front of the detector and lock-in amplification enables simultaneous determination of several elements of the scattering matrix, F_{ij}, with a high signal-to-noise ratio. The scattering matrix $\boldsymbol{F}(\lambda, \theta)$ of a cloud of dust particles is a 4×4 matrix defined by the following equation:

$$\boldsymbol{s}_{\rm sca}(\lambda, \theta) = \frac{\lambda^2}{4\pi^2 D^2}\boldsymbol{F}(\lambda, \theta)\,\boldsymbol{s}_{\rm inc}(\lambda, \theta), \quad (1)$$

where the Stokes vectors of the incident beam ($\boldsymbol{s}_{\rm in}$) and the scattered beam ($\boldsymbol{s}_{\rm sca}$) define their respective fluxes and states of linear and circular polarization. In Equation (1), θ is the scattering angle (the complementary angle of the phase angle, α), λ is the wavelength, and D is the distance to the detector. For clouds of randomly oriented particles with mirror symmetry, there are only six independent nonzero elements forming a block-diagonal scattering matrix (Muñoz et al. 2011).

In the present work, we report measurements of $F_{11}(\theta, \lambda)$ and $-F_{12}(\theta, \lambda)/F_{11}(\theta, \lambda)$, which are the only scattering matrix elements that can be observed by passive remote sensing. The function $F_{11}(\theta, \lambda)$ corresponds to the phase function and is proportional to the flux of the scattered light for unpolarized incident light. Also, for unpolarized incident light, the ratio $-F_{12}(\theta, \lambda)/F_{11}(\theta, \lambda)$ is called the DLP. The measurements have been carried out at a single visible wavelength: $\lambda = 514$ nm.

This setup can be used to measure the scattering matrix as a function of the scattering angle of clouds of randomly oriented micron-sized particles, created by an aerosol generator (Muñoz et al. 2011). The aerosol generator consists of a cylindrical stainless-steel dust container with a plunge rod that is moved upward (speed <100 mm hr^{-1}) and pushes the powder toward a stainless-steel rotating brush, which entrains the particles in an air stream that carries the particles and delivers them through a nozzle at the center of the experiment. Single scattering conditions in this setup have been demonstrated elsewhere (Muñoz et al. 2011). The rotating brush also has the effect of disaggregating any particle agglomerates that may form in the reservoir.

3. Sample Characterization

3.1. Optical Constants

The HAC samples generated in our experiments show characteristic IR absorptions of Csp^2 and Csp^3 bonds (see below). The optical constants between the near-UV and the near-IR (NIR) are determined by the weaker bound π-electrons of the graphitic sp^2 bonds. Thus, changes in the sp^2/sp^3 ratio caused by different environmental conditions have an impact on the imaginary part of the refractive index of HAC. The absorptivity depends on the size of the largest aromatic clusters embedded in the structure of the solids. The incorporation of hydrogen into the structure also has an influence on the optical constants because the inclusion of hydrogen favors Csp^3 bonding, limiting the size of the graphitic domains, and thus, decreasing absorption (Compagnini et al. 1995; Hony et al. 2003).

We have carried out transmission spectroscopy measurements in order to determine the optical constants n and k (i.e., the real and imaginary parts of the complex refractive index, $m = n + ik$) of the carbonaceous dust analogs generated in this work. The determination of the optical constants by transmission spectroscopy is challenging because the morphology of the dust results in a significant contribution of scattering to extinction. To minimize scattering effects, several KBr pellets containing about 1% in weight of HAC or HAC + forsterite powder were produced.

However, this was not enough to permit a reliable determination of the real part of the refractive index, n. This parameter has been extensively analyzed in the literature, and some of these data are included in the Heidelberg–Jena–St. Petersburg database of optical constants (HJPDOC; Henning et al. 1999).[5] In Table 1 we have compiled a list of works that analyze this parameter. For instance, in the case of hydrogenated carbonaceous films, Godard & Dartois (2010) analyzed a set of experimental data, which allowed them to identify a relationship between n and the band-gap energy. Jacob (1998) examined the optical properties of hydrocarbon films generated in low-temperature hydrocarbon plasmas and found a relationship between n and the material density ρ. Subsequently, Kassavetis et al. (2007) also analyzed this correlation and obtained the following relation: $n^2 = 1 + 1.85\ \rho$. Peláez et al. (2018) studied hydrocarbon films produced in an RF inductive discharge and used independent experimental techniques to measure the band-gap energy. A n value of 1.7, and a density of 1.1 g cm^{-3} were obtained, in agreement both with Kassavetis and Jacob's correlations. Furthermore, the measurement of the band-gap energy supports the value of n obtained based on the relation described by Godard & Dartois (2010). Smith (1984) examined the optical properties of thin films at various annealing temperatures. In both cases, a decrease in the optical

[5] https://www.astro.uni-jena.de/Laboratory/OCDB/index.html

Table 1
Optical Constants of Different HAC Materials Reported in the Literature

Method	Precursors	n	k	Reference
DC glow discharge. Annealing: 250°C–750°C	C_2H_2	1.74–2	6.5×10^{-3}–0.8	Smith (1984)
RF discharge	CH_4	1.59–2.13	1.5×10^{-2}–5.7×10^{-2}	Jacob (1998)
Pyrolysis @ 400°C	Cellulose	1.57	0.41	Jager et al. (1998)
Sputtering, PECVD, FCVA, PLD	Graphite, C_6H_6, C_2H_2,	1.6–2.7		Kassavetis et al. (2007)
DC discharge (550 V)	Graphite + Ar	1.7	5×10^{-2}	Zeinert et al. (2008)
Evaluation of experimental data		1.4–2.3		Godard & Dartois (2010)
Inductive RF discharge (13.56 MHz, 40 W)	CH_4/He	1.7–1.75	$<5 \times 10^{-4}$	Peláez et al. (2018)
Plasma-assisted chemical vapor deposition 25°C–300°C	CH_4/Ar	1.57–1.75	1×10^{-3}–3×10^{-2}	Jaglarz et al. (2020)
Capacitive RF discharge (13.56 MHz, 15 W, 80 minutes, modulated)	C_2H_2/Ar	1.7	$<3 \times 10^{-2}$	This work

gap was observed, indicating that dehydrogenation and graphitization processes result in an increase of both n and k.

Although most experiments have been conducted on thin films, work on morphologies closer to those expected in cosmic dust has also been conducted. Jager et al. (1998) studied the optical indices of pyrolyzed cellulose at different temperatures and Zeinert et al. (2008) analyzed the optical properties of porous carbonaceous particles with a mean diameter of 54 nm, produced in Ar sputtering DC discharges. They obtained a refractive index value of $n = 1.7$ with very low absorbance. This value is comparable to those obtained by other authors for thin films. Hence, a value of $n = 1.7$ has been assumed in this work.

Regarding the imaginary part of the refractive index, our measurements of normal transmittance spectra of the KBr + HAC pellets from the visible to the mid-infrared (MIR) spectral range have enabled us to derive k using the Beer–Lambert law. In the visible range, the transmission spectra were recorded between 500 and 700 nm with an optical microscope (BS-1053 PLMI) coupled via an optical fiber to a UV-Vis spectrometer (Ocean Optics, model QE65000). The 12 mm diameter KBr pellets were sampled in four different positions to account for the inhomogeneity of the mixture along the pellet. The HAC + forsterite samples were more transparent to the visible radiation, and the absorbance was below the sensibility of our instrument. The visible k values obtained for HAC are shown in Figure 1, where the uncertainties originate mainly from the estimation of the HAC effective thickness and the inhomogeneity of the dust distribution within the KBr pellet. The effective thickness is obtained from the relative density and mass of HAC and KBr, resulting in a value of 5 μm, compared to the 720 μm of the pellet. The contribution of scattering to extinction (although minimized) is a systematic uncertainty that cannot be quantified, and hence the values in Figure 2 are, strictly speaking, upper limits. The k values obtained at 633 nm are close to the values obtained for other HAC materials with hydrogen atomic fractions $x_H \sim 0.3$–0.4 (Dischler et al. 1983; Compagnini et al. 1995).

Transmission spectra of the same pellets were recorded with a Bruker Vertex-70 FTIR spectrometer in the infrared range between 4000 and 550 cm^{-1} (0.71–18 μm). The main absorption features appear in the MIR region and are shown in Figure 2. The HAC IR absorption features observed agree with typical features of interstellar carbonaceous analogs (Pendleton & Allamandola 2002). Specifically, the band centered around 2900 cm^{-1} (~3.4 μm), which corresponds to the asymmetric stretching of the aliphatic CH_3 and CH_2 groups, the bands at 1450 (~6.9 μm) and 1370 cm^{-1} (~7.3 μm) are attributed to the deformation modes of CH_2 and CH_3, respectively, and a broad band around 1600 cm^{-1} (~6.2 μm) assigned to aromatic (mostly) and olefinic C=C stretching modes. Inspection of

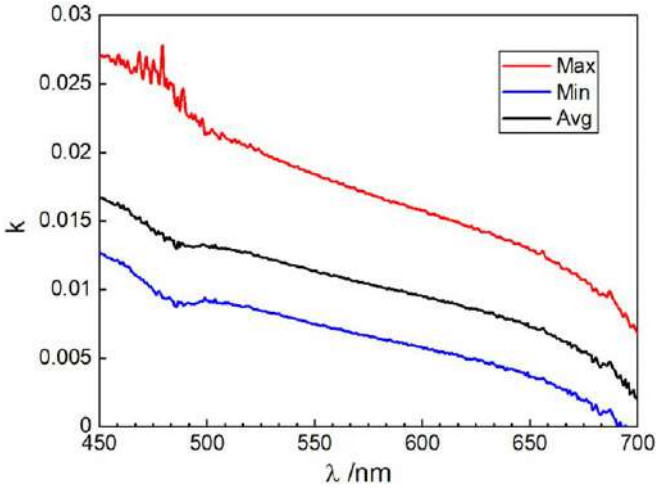

Figure 1. Imaginary part of the refractive index, k, of HAC estimated from transmission spectroscopy measurements on HAC + KBr pellets. The black solid line indicates the values of k obtained from the averaged transmittance spectrum (spectral scans at four different points of the KBr pellet). The red and blue lines correspond, respectively, to the values of k obtained from the minimum and maximum measured transmittances.

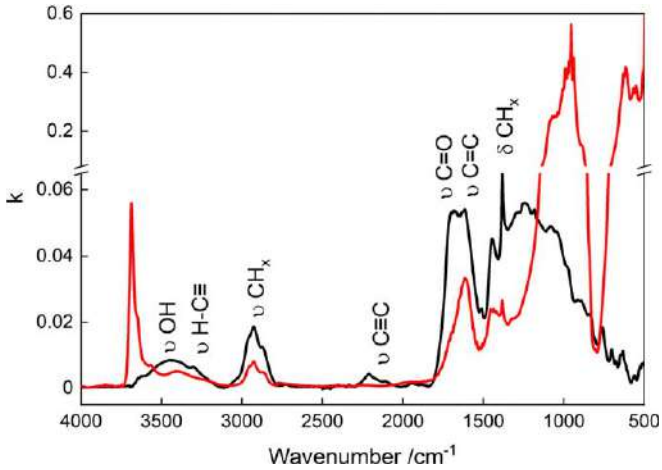

Figure 2. Imaginary part of the refractive index of HAC (red line) and HAC + forsterite (black line) powders, estimated from absorption spectroscopy measurements on pellets using KBr as a substrate. Note the break in the vertical axis. The main vibrations appearing in the HAC spectrum are identified by standard Greek symbols (υ, stretching; δ, bending).

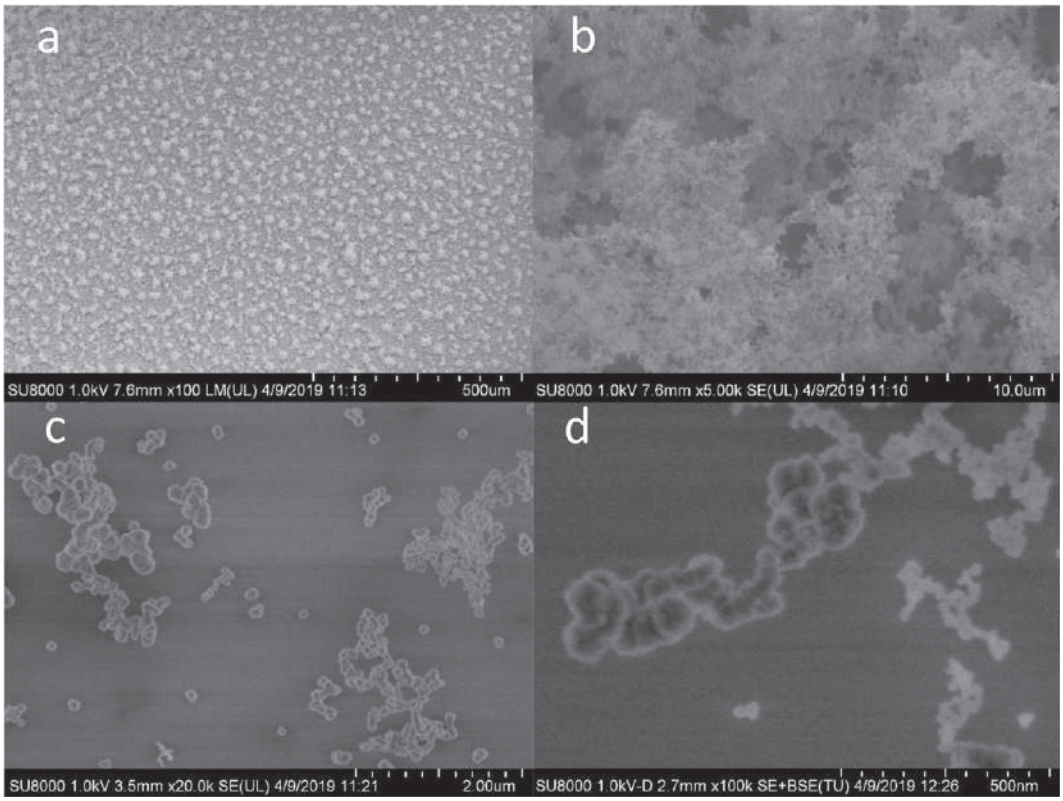

Figure 3. SEM images of an HAC sample directly grown on an Al substrate in the RF discharge reactor. The dimensions are indicated in the corresponding panels.

these bands points to a high proportion of polyaromatic (Csp^2) structures. Some oxygen contamination gives rise to OH and CO bands at 3500 cm^{-1} (∼2.9 μm) and 1700 cm^{-1} (∼5.9 μm), respectively. The HAC + forsterite samples show stronger absorptions than HAC, with the main peaks appearing at 1000 cm^{-1} (∼9.7 μm) due to Si–O stretching and at 555 cm^{-1} (∼18 μm) caused by O–Si–O bending (O'Donnell 1994; Ghahari & Naeimi 2017). Also, a small band at 3600 cm^{-1} (∼2.8 μm) appears, corresponding to the O–H stretching mode and likely related to moisture. The NIR measurements of 14,000–4000 cm^{-1} (0.71–2.5 μm) do not show any significant absorptions neither in pure HAC nor in the HAC + forsterite samples and therefore are not shown in the figure.

For crystalline forsteritic olivine, there is a refractive index at 633 nm of $m = 1.6 + i3 \times 10^{-5}$ from the HJPDOC, which is consistent with the low k value in the visible range suggested by our experiments.

3.2. Particle Morphology

SEM images of HAC materials deposited on the Al substrates located on top of the bottom electrode are shown in Figure 3. It can be seen that HAC is a porous material composed of micron-sized aggregates (Figures 3(a) and (b)) of nanometer-sized subspherical monomers (Figures 3(c) and (d)). The aggregate particles are formed by chains of monomers with radii of a few tens of nanometers. A few free monomers can be observed (Figure 4(c)). These SEM images (Hitachi SU8000) were obtained without applying the usual gold coating, which can be a problem for dielectric particles, which easily charge with the electron beam, but has the advantage of enabling a more detailed view of the particles' surfaces, which show a *cauliflower* structure. In Figure 3(d), the smallest monomers have a radius of ∼ 10 nm, with larger compact particles ($r \sim$ 50 nm on average), possibly formed by aggregation of smaller monomers (hence the cauliflower structure).

As mentioned above, the HAC sample used in this study for scattering matrix measurements was recovered from both the surface of the lower electrode and the inner walls of the reactor and consists of a fluffy network of monomers. During the scattering measurements, a fraction of the HAC sample ejected by the aerosol generator was collected on the surface of an SEM pin stub placed directly below the stream of particles. This was done to ensure that the particles probed by the scattering laser are the same as those collected on the pin stub, which were observed later ex situ by SEM (Zeiss Gemini Field Effect SEM). Figure 4 shows SEM images of these particles, which are aggregates containing monomers that are on average 60 nm in radius (Figure 4). This average radius agrees, within uncertainty, with the radius estimated for particles directly deposited on an aluminum substrate in the plasma reactor (Figure 3(d)). Figure 4(b) shows a typical aggregate particle with dimensions of a few microns. These structures are consistent with cluster-cluster aggregates (Bertini et al. 2009) and resemble those shown in Figure 3(b).

SEM images of the pure forsterite XS sample can be found in Figure 3 of Muñoz et al. (2021). The particles of this sample are compact with irregular shapes and tend to stick to each other as a result of electrostatic forces. However, in the mixture with HAC, the forsterite particles do not appear clumped. Larger forsterite particles appear covered by HAC (Figures 5(a) and (b)), while small forsterite particles are embedded in the HAC network (Figures 5(c) and (d)). This can be observed more clearly in transmission electron microscopy images (Figure 6), where the green and yellow EDX compositional

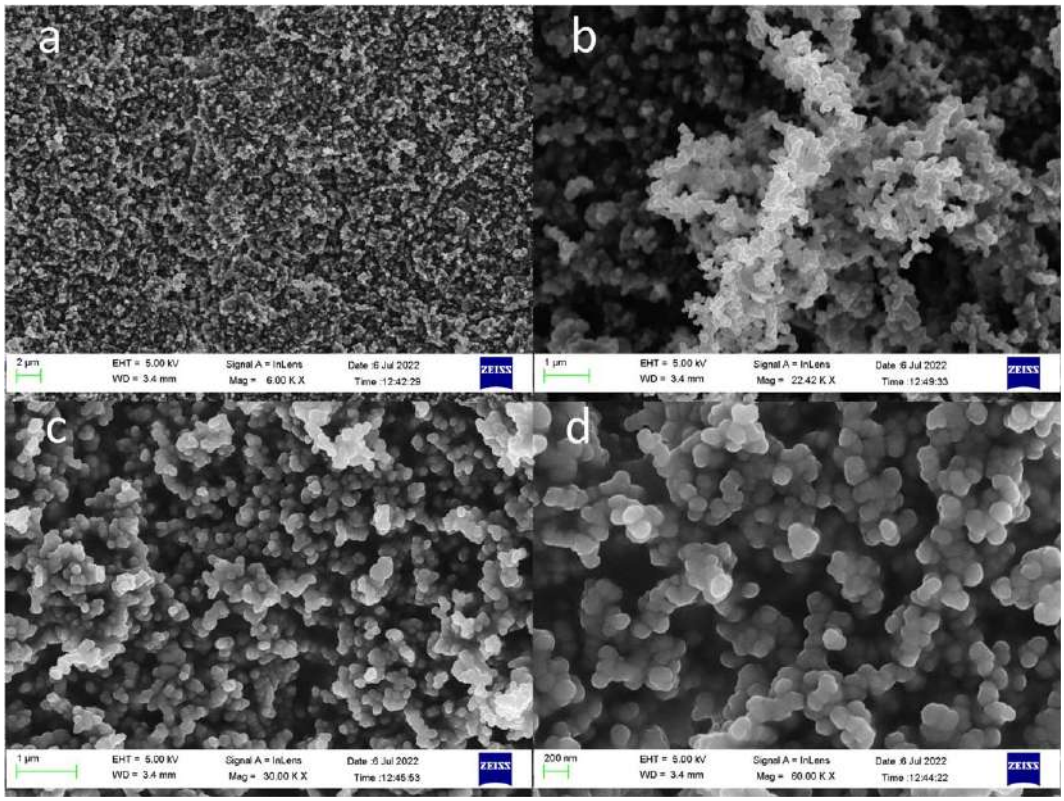

Figure 4. SEM images of the HAC sample at magnifications of $\times 6 \times 10^3$ (panel (a)), $\times 2.242 \times 10^4$ (panel (b)), $\times 3 \times 10^4$ (panel (c)), and $\times 6 \times 10^4$ (panel (d)). The images were obtained from particles deposited on an SEM sample holder from the cloud generated by the aerosol generator in CODULAB.

maps indicate the distribution of carbon and silicon atoms, respectively.

3.3. Particle Size

The particle size distributions (PSDs) of the pure HAC and HAC + forsterite samples were measured using a laser light-scattering (LLS) particle-sizing apparatus (Malvern Mastersizer 2000). The *measured* PSD of a particulate sample corresponds to the size distribution of projected surface-equivalent spheres. We have previously established that this technique operates reliably using the Mie model for spherical particles with radii $r > 0.1\,\mu$m, while for $r \leqslant 0.1\,\mu$m the inversion is ill-conditioned. Moreover, for irregular particles, care must be taken when interpreting the results in the $0.2\,\mu\text{m} < r < 1\,\mu$m range (Gómez Martín et al. 2020).

The PSDs of the HAC and HAC + forsterite samples were obtained by diluting a fraction of the powder in a non-polar fluid (toluene, $n = 1.4969$) to hinder the formation of large van der Waals agglomerates. Mie theory was employed in the determination of the PSDs, using m (633 nm) $= 1.70 + i0.015$ (k near the upper limit in Figure 1) and m (466 nm) $= 1.70 + i0.03$ for the HAC sample. For the HAC + forsterite 50wt%. mixture, a refractive index estimated using the Bruggeman mixing rule was considered ($m = 1.68 + i0.01$ at 633 nm and $m = 1.68 + i0.02$ at 466 nm). The logarithmic-scale number PSDs, $N(\log r)$, are plotted in Figure 7(a) (note that $N(\log r)\, d\log r$ is the fraction of the total number equivalent spheres in the size range between $\log r$ and $\log r + d\log r$). The number of PSDs of the HAC and the HAC + forsterite samples shows a mode for $r > 0.4\,\mu$m with a maximum at $r \sim 0.6\,\mu$m, and a mode for $r < 0.4\,\mu$m with a maximum at $r \sim 0.025\,\mu$m (red and black lines in Figure 7(a)). As mentioned above, the LLS measurements of the PSD of irregular particles at 633 nm need to be considered with caution for $r < 1\,\mu$m, and in particular, the values for $r < 0.1\,\mu$m are usually wrong. Note that Figure 3 shows that besides aggregates some loose HAC monomers exist, perhaps as many as 10 for each aggregate, which is a significantly lower ratio than derived from the particle sizer distribution (ratio 10,000:1, see the red line in Figure 7(a)). There is a clear separation between spurious and valid data at $0.4\,\mu$m, where $N(\log r) = 0$. We therefore truncate the PSDs of the HAC and the mixed sample and consider as valid only the curves for $r > 0.4\,\mu$m (Figure 7). The origin of the spurious small particle mode is discussed in Section 5 in the context of assessing the effects of assuming spherical geometry to interpret scattering data of irregular particles.

The PSDs of the HAC and the mixed samples for $r > 0.4\,\mu$m are almost identical, which indicates that the mixture does not contain free forsterite particles, but they are incorporated into the HAC aggregates as shown in Figure 6. Hence, the mixed sample can be considered an internal mixture. The effective radii (r_{eff}) and standard deviations (σ_{eff}) (as defined by Hansen & Travis 1974) of the PSDs of the three samples are listed in Table 2.

4. Experimental Phase Function and DLP

The experimental phase function and DLP curves of the HAC and the HAC + forsterite samples are plotted against the scattering angle θ in Figure 8 alongside the corresponding curves of the forsterite sample previously reported by

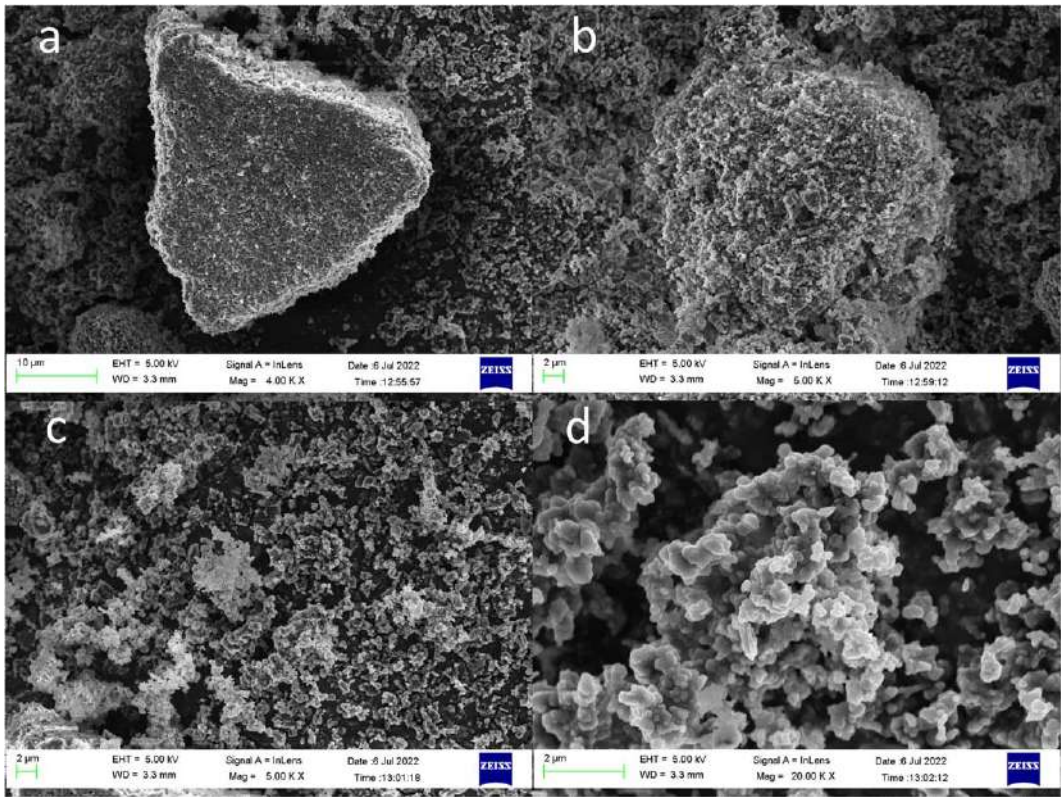

Figure 5. SEM images of the HAC + forsterite 50wt% sample at magnifications of $\times 4 \times 10^3$ (panel (a)), $\times 5 \times 10^3$ (panels (b) and (c)), and $\times 2 \times 10^4$ (panel (d)). The images were obtained from particles deposited on an SEM sample holder from the cloud generated by the aerosol generator in CODULAB.

Muñoz et al. (2021). Scattering parameters derived from the measured curves are listed in Table 3.

The phase function of the HAC sample is flat at the side and near the backscattering angles (90°–160°) and shows a modest enhancement of backscattering ($\theta > 165°$). The phase function of the mixed sample is closer to that of the forsterite sample at the side and near the backscattering, with a steeper angular dependence. Q-space analysis of the phase functions (log–log scale plot of the phase function versus the scattering wavevector $q = (4\pi/\lambda)\sin(\theta/2)$ shown in the insert of Figure 8(a) for HAC (Sorensen et al. 2017), shows extensive linear regions similar to other samples of the Granada–Amsterdam database (Muñoz et al. 2012). The slopes of the phase functions of the HAC, forsterite, and mixed samples are listed in Table 3. Regarding the DLP, the HAC curve is bell-shaped and symmetrical (maximum DLP at $\theta = 90°$) and resembles the angular dependence of the DLP in the Rayleigh scattering regime (the black curve in Figure 8(b), (Hansen & Travis 1974), although a hint of a negative polarization branch (NPB) can be observed (insert panel in Figure 8(b)). By contrast, the HAC + forsterite mixture shows an asymmetric DLP curve peaking at $\theta = 100°$ and a deeper NPB with a minimum of 2%–4% at $\theta = 167°$, similar to the pure forsterite behavior. In general, the curves of the mixture lie between the curves of the pure samples, although the scattering behavior of the mixture is closer to that of the forsterite sample.

5. Discussion

5.1. Simple Models of Porous Aggregate Samples

To avoid overparameterization, astronomical observations are often modeled using simplified particle models, including spheres, hollow spheres, and ellipsoids, in combination with optical constants derived from effective medium theories. It is well known that the full scattering matrix of porous aggregates cannot be reproduced accurately using such simplified models (Voshchinnikov et al. 2005), but it is useful to explore what kind of deviations from the actual particle size and optical constants can be expected when such models are applied to real laboratory samples.

We have carried out Mie calculations (Mishchenko et al. 2002) using a multimodal volume log-normal distribution that represents well the PSD of our HAC sample. Considering a porosity of 60% (calculated from the SEM image in Figure 4(c) using an area-based porosity estimation code that separates material and pores by thresholding and segmentation of the image) and $m(514\text{ nm}) = 1.7 + i0.015$, an effective refractive index $m(514\text{ nm}) = 1.3 + i0.007$ is estimated using the Bruggeman mixing rule (Voshchinnikov et al. 2007). With the measured PSD for $r > 0.4\ \mu$m (red line in Figure 7), the calculated F_{11} curve for spheres (Figure 9(a), dashed black line) fits well the measured data for $3° \leqslant \theta \leqslant 30°$, but the same is not true for the DLP curve (Figure 9(b), dashed black line). The disagreement remains for other values of porosity within the 50%–70% range estimated from Figure 4(c). We find that, in order to improve the agreement between the calculated and the measured curves for a wider range of scattering angles, an unrealistically high number of small particles (3–4 orders of magnitude more monomers than aggregates) must be artificially included in the PSD, even though there is evidence from the SEM images that they are not dominant. Thus, adding a mode of monomer-sized particles to the PSD ($r_g \sim 60$ nm, ln $\sigma_g \sim 0.16$) improves the agreement between the simulated and experimental F_{11} curves, extending the agreement to

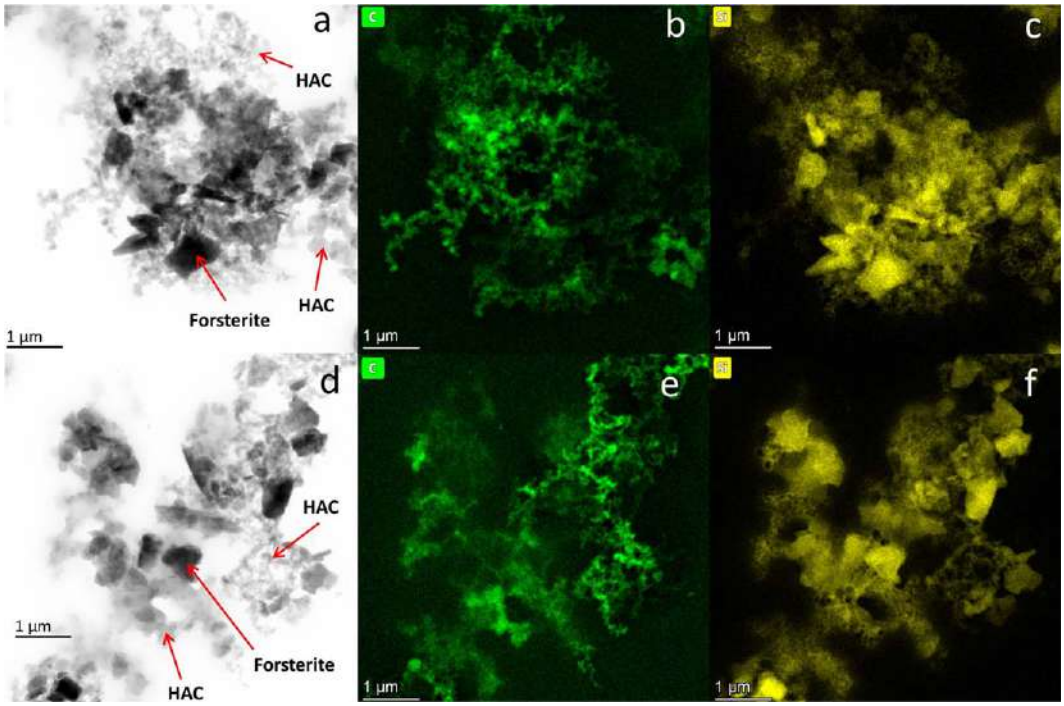

Figure 6. TEM high-angle annular dark-field imaging (HAADF) (panels (a) and (d)) and EDX analysis (panels (b), (c), (e) and (f)) of two mixed agglomerates of forsterite and HAC. In the HAADF images forsterite grains appear as dark angular fragments with sizes between 0.1 and 1 μm embedded in chain-like structures of HAC composed of spherical monomers with diameters smaller than 0.2 μm. The green and yellow EDX compositional maps indicate the distribution of carbon and silicon atoms, respectively.

$3^\circ \leqslant \theta < 50^\circ$ (Figure 9(a), dashed blue line). Also, as a consequence of this, the shape of the calculated DLP curve becomes qualitatively comparable to that of the measured one, but with a too large $P_{\max}$ (Figure 9(b), dashed blue line). Better agreement with the $P_{\max}$ value is found by shifting the small particle mode to a larger average radius ($r_g \sim 100$ nm) and making it broader ($\ln \sigma_g \sim 0.3$) (Figure 9(b), solid blue line), and using a refractive index within the range estimated for HAC in Section 3.1 ($m(514\text{ nm}) = 1.7 + i0.015$). Note that it is even possible to match the measured $P_{\max}$ with a size distribution containing only small particles with $r_g \sim 100$ nm (size parameter $x \sim 1$) (Figure 9(b), solid red line).

In view of the relatively low number of loose monomers observed in the SEM images, the discussion above suggests that the scattering properties of our HAC sample at the side scattering angles (especially the DLP) are strongly influenced by particles tens to hundreds of nanometers in radius that are embedded within the observed aggregates. In other words, the internal structure of the aggregates determines the scattering properties at the side scattering angles and the overall size of the aggregates determines the phase function in forward scattering. Rayleigh–Ganske–Debye (RGD) theory is often invoked when porous aggregates behave almost like an ensemble of their individual constituent monomers in terms of light scattering (Tazaki et al. 2016). Under RGD conditions, the slope of the log–log Q-space plot corresponds to the fractal dimension D_f of the aggregates and this remains approximately true for an ensemble of polydisperse aggregates (Sorensen 2001). The Q-space slope of the HAC sample is significantly lower than 2, which in fact is consistent with low fractal dimension and high porosity. However, our HAC sample does not fulfill the RGD conditions: the real part of the refractive index is too high, the monomers are not Rayleigh particles, and the aggregates are not far from the geometric optics regime. Note that even though it is possible to obtain a reasonable approximation of the phase function combining aggregates with monomers of the observed size (dashed line in Figure 9(a)), the $P_{\max}$ of the separate monomers is way too high (dashed line in Figure 9(b)). Ultimately the best model contains spherical monomers that are larger ($r > 100$ nm) than observed ($r \sim 60$ nm). This is because for $r > 100$ nm the maximum of the bell-shaped DLP curve of spheres starts to decrease significantly with increasing parameter size, which facilitates matching measured curves of lower $P_{\max}$ with the calculated curves. However, the actual explanation for a low DLP of the aggregate compared to the ensemble of monomers is that depolarization occurs within the HAC aggregates (Tazaki et al. 2016).

A similar exercise can be carried out using the so-called distribution of hollow spheres (DHS) (Min et al. 2005) using the code of Toon and Ackerman for two-layered spheres (Toon & Ackerman 1981), where the inner layer (the core) is assigned a refractive index of $m = 1 + i0$. In this case, the agreement is better for the DLP(θ) curve, but this also requires the presence of an unrealistic mode of small monomer-sized particles. Again, it is possible to obtain a calculated DLP curve reasonably close to the measured one without including the aggregates in the PSD. Min et al. (2005) hypothesized that the presence of a mode of small particles in the PSD retrieved with the DHS model could either result from real particles that were not observed by diffraction-based (Fraunhofer) particle sizes, or from the fitting procedure trying to simulate scattering by small-scale structures in the particles. Inspection of Figures 3(c) and (d) indicates that there are no large amounts of loose monomers in the HAC sample, which supports the interpretation of the small particle mode as representative of the monomers embedded in the aggregate structure of the particles.

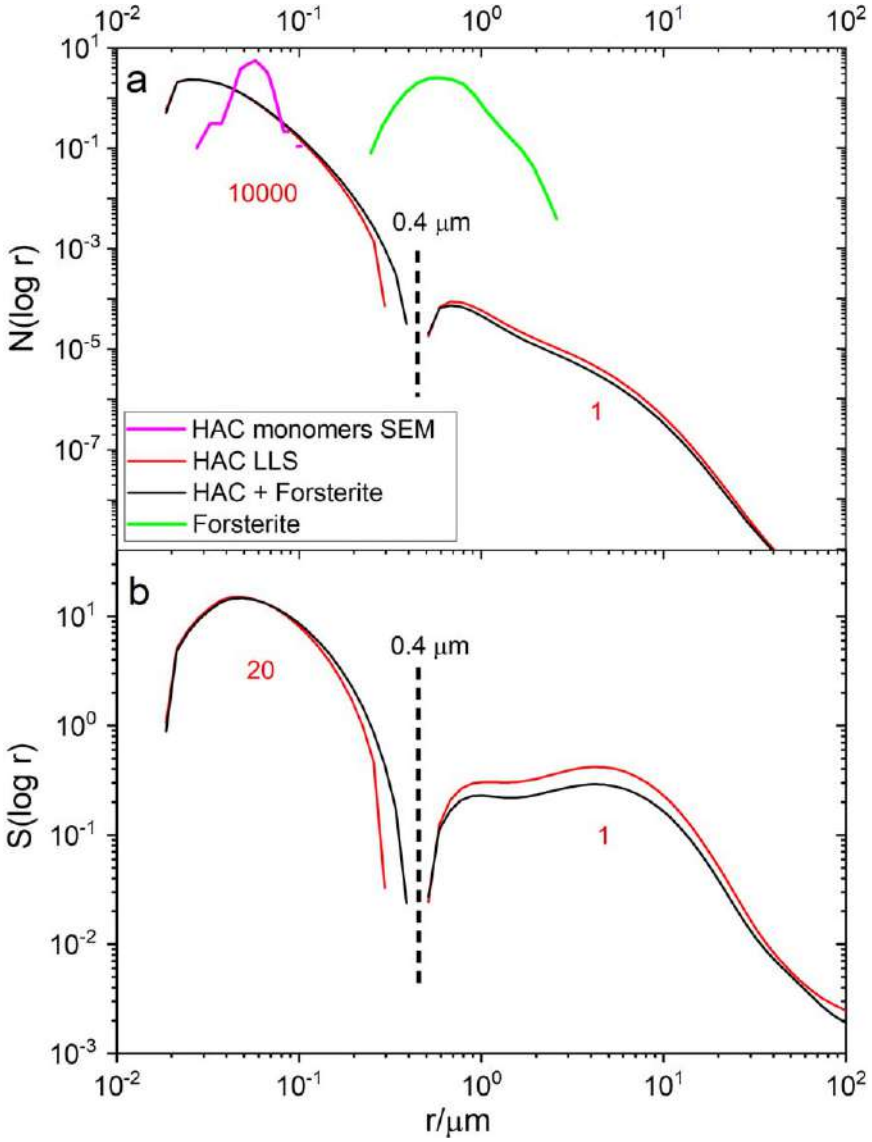

Figure 7. (a) Normalized logarithmic-scale number PSD $N(\log r)$ of monomers and aggregate particles of HAC and forsterite. Pink line: distribution of 245 spherical HAC monomers found in the SEM images in Figures 4(b) and (c). Green line: forsterite PSD (Muñoz et al. 2021). Red line: PSD of the pure HAC sample as measured by LLS using $m(633\ \text{nm}) = 1.7 + i0.015$ and $m(466\ \text{nm}) = 1.7 + i0.03$. Black line: PSD of the HAC + forsterite sample as measured by LLS using $m(633\ \text{nm}) = 1.66 + i0.01$ and $m(466\ \text{nm}) = 1.66 + i0.02$. (b) Logarithmic-scale normalized projected surface PSD $S(\log r)$ corresponding to the HAC and HAC + forsterite number PSDs in panel (a). The numbers under the curves indicate the relative contribution to the number of particles and surface for $r < 0.4\ \mu$m and $r > 0.4\ \mu$m.

Table 2
Average Radius ($\bar{r}$), Standard Deviation (σ), Effective Radius (r_{eff}), and Effective Standard Deviation (σ_{eff}) (Hansen & Travis 1974) of the HAC and HAC + Forsterite Samples ($r > 0.4\ \mu$m) and the Forsterite Powder

Sample	$\bar{r}/\mu$m	σ	r_{eff}/μm	σ_{eff}	Reference
HAC	1.2	0.9	5.0	1.5	This work
Forsterite	0.5	0.3	0.6	0.4	Muñoz et al. (2021)
Mixture 50wt%	1.2	0.9	5.1	1.7	This work

In summary, quantitative agreement cannot be obtained for the phase function and DLP curves simultaneously with common parameters using the simplistic models above. The spherical model blurs the distinction between aggregates and monomers and results in an underestimation of the *real* particle size through the artificial introduction of small particles. In addition, these models may also lead to an overestimation of the size of the monomers.

5.2. Testing the Effect of Assuming Spherical Geometry in the Retrieval of Dust Particle Sizes from Phase Function Measurements

The LLS method is based on the inversion of the phase function measured at small scattering angles at $\lambda = 633$ nm using a scattering model (Fraunhofer or Mie). The technique is based on the assumption that the forward diffraction peak is mainly dependent on particle size and not on particle shape (Mishchenko 2009). Some LLS particle sizers include large angle detectors as well as an additional laser beam ($\lambda = 466$ nm in the Mastersizer 2000), to gain sensitivity toward the submicron size range. Therefore, the LLS performs measurements of the phase functions shown in Figure 8(a) at selected angles and uses inverse modeling to derive the PSD considering spherical geometry. In Section 5.1 we have performed forward modeling to show that the modeling of the phase function and the DLP with spheres requires an

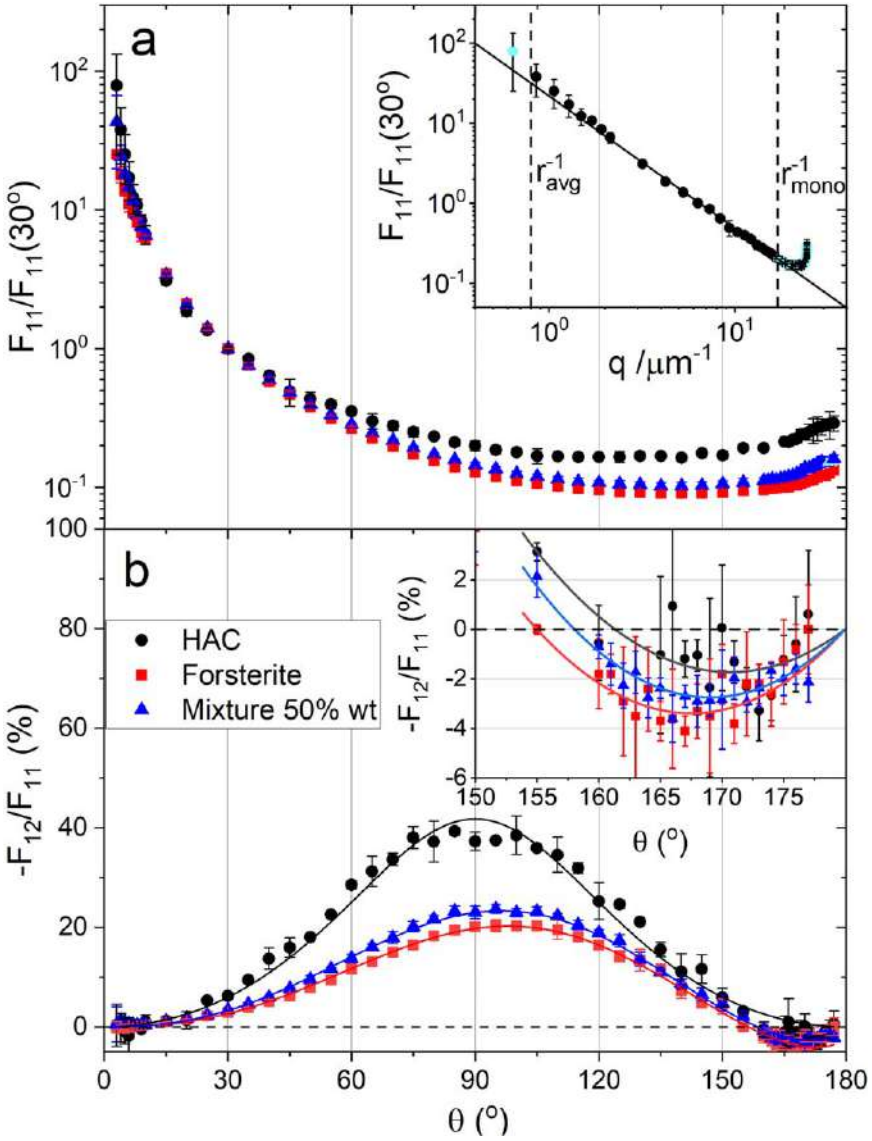

Figure 8. Experimental phase function (panel (a)) and DLP (panel (b)) of the HAC, forsterite, and mixed samples vs. the scattering angle θ at 514 nm. The F_{11} curves are normalized to the value at $\theta = 30°$. The insert in panel (a) shows a Q-space analysis (Sorensen et al. 2017) of the HAC phase function with the corresponding power-law fit (the cyan symbols are outside of the power-law regime defined by the reciprocal average radius of aggregates and the radius of monomers and are therefore masked). The insert in panel (b) shows the near-backscattering region of the DLP curve. The black solid line in panel (b) corresponds to the angular dependence of the Rayleigh scattering DLP (Hansen & Travis 1974) scaled to match the DLP of the HAC sample. The red and blue solid lines represent empirical fits of the Lumme & Muinonen expression (Kiselev et al. 2015) to the DLP curves of the forsterite sample and the mixed sample, respectively. The solid lines in the insert panel represent empirical parabolic fits of the NPB of the three samples.

unrealistic number of small particles to come closer to the measured curves. Hence, one could expect the same effect in the particle-sizing method.

In fact, the large number of small particles for $r < 0.4\ \mu$m retrieved for the HAC and HAC + forsterite samples (Figure 7), which we have discarded in Section 3.3 based on previous work (Gómez Martín et al. 2020), is a manifestation of the exact same problem highlighted above. The area under the $N(\log\ r)$ curve in Figure 7(a) for $r < 0.4\ \mu$m would be the number of spheres with $r < 0.4\ \mu$m, which would be four orders of magnitude larger than the number of spheres with $r > 0.4\ \mu$m. Figure 3 shows that even though some loose HAC monomers exist, perhaps as many as 10 for each aggregate, they are not in the 10,000:1 ratio indicated by the PSD. The spurious small particle mode appears as a result of the low side-scattered intensity predicted by the Mie model used by the LLS method, compared to the shallow measured phase function for irregular particles such as the HAC aggregates. This mismatch is balanced in the optimization procedure implemented in the analysis software of the LLS instrument by a large number of small particles, which improves the fit of the phase function, but produces incorrect PSD values for $r < 0.4\ \mu$m.

For the purpose of estimating the effect of the loose monomers, we may attempt to reconstruct the real PSD of the sample assuming that the loose monomers are in a 10:1 ratio to the aggregates, as suggested by the SEM images (Figure 3(c)). Under this assumption, the number size distribution would look like the one in Figure 10(a), where we have concatenated the monomer size distribution from the SEM images in Figures 4(b) and (c) with the truncated LLS number distribution. The corresponding projected surface distribution $S(\log\ r)$ is shown in Figure 10(b). The projected surface of the r

Table 3
Scattering Parameters of the Samples

Sample	$F_{11}(10°)/F_{11}(90°)$[a]	p[b]	$F_{11}(174°)/F_{11}(150°)$[c]	P_{min} (%)	θ_{min}[d] (deg)	P_{max}[e] (%)	θ_{max}[e] (deg)
HAC	33 ± 6	−1.654 ± 0.016	1.61 ± 0.24	1.7 ± 0.7	172 ± 3	42 ± 4	90 ± 3
Forsterite	48 ± 3	−2.023 ± 0.013	1.44 ± 0.14	3.4 ± 1.0	167 ± 3	20 ± 1	98 ± 3
Mixture	45 ± 3	−1.894 ± 0.012	1.44 ± 0.14	2.7 ± 1.0	169 ± 3	23 ± 1	97 ± 3

Notes. P_{min} is the minimum DLP at scattering angle θ_{min} (in the NPB) and P_{max} is the maximum of polarization at phase angle.
[a] Ratio of values of the phase function at different scattering angles used by Volten et al. (2007) to quantify the steepness of the phase function of porous silicate aggregates.
[b] Slope of the Q-space log–log plot (insert Figure 8(a)).
[c] Enhancement of the backscattering ratio.
[d] From empirical parabolic fits of the NPB.
[e] From empirical fits to the full DLP curves (see text).

$\sim$ 60 nm monomers (size parameter $x = 2\pi r/\lambda \sim 1$ at $\lambda =$ 514 nm) is about 80 times lower than the projected surface of aggregates. This, combined with the low scattering efficiency of $x \sim 1$ particles relative to particles with $x \sim 10$ ($r = 1$ μm at $\lambda = 514$ nm) (Hansen & Travis 1974), indicates that the loose monomers have a negligible impact on the light scattered by the HAC sample.

5.3. Comparison with Other Circumstellar Dust Analogs

A few experimental studies of the light-scattering behavior of cosmic dust analogs generated by bottom-up methods (i.e., gas-to-particle conversion reactors) have previously been reported (Hadamcik et al. 2002, 2006, 2007; Volten et al. 2007). In these studies, CB particles were used as carbonaceous dust analogs. CB is a highly absorbing material consisting of a mixture of graphitic and partially dehydrogenated amorphous carbon (Zerda et al. 1998). The CB particles are composed of monomers with sizes between 10 and 100 nm, which are fused together forming porous aggregates in a similar way to HAC.

The polarization curve measured at 543.5 nm for CB agglomerate particles with sizes between 10 and 70 μm, containing aggregate subunits with sizes between 0.5 and 2.5 μm, and ultimately composed by monomers with size 95 ± 20 nm (i.e., 0.5 μm $< r_{aggr} <$ 2.5 μm, $r_{monom} \sim 50$ nm) is similar to the DLP curve of the HAC sample reported here, with $P_{max} = 44\%$. The main difference between the two curves is the asymmetry of the CB curve, which peaks at $\theta = 70°$. The DLP of CB was measured by lifting the particles in an air draft, where they agglomerated forming much larger particles than the 0.5–2.5 μm aggregates (Hadamcik et al. 2006). Although P_{max} is expected to depend to a large extent on the size of the monomers, P_{max} is slightly lower for larger agglomerates tens of microns in size (Hadamcik et al. 2007), as a result of multiple scattering. This effect might be balanced by the higher P_{max} that can be expected for the more absorbing CB particles, which would explain why the P_{max} is similar to that of our HAC sample.

Porous aggregate particles composed of silica and magnesium, iron and aluminum silicates, and oxides have also been investigated (Hadamcik et al. 2006, 2007; Volten et al. 2007). The DLP curves measured for these particulate samples at $\lambda = 633$ nm are bell-shaped and peak at 90°. The HAC sample has a lower phase function steepness ($F_{11}(10°)/F_{11}(90°)$), higher enhancement of backscattering ($F_{11}(174°)/F_{11}(150°)$), and lower P_{max} (Table 3) than the magnesium silicate, ferrosilicon, and alumina aggregates studied by Volten et al. (2007) The effects of several variables (monomer size, porosity, optical constants) are entangled in the scattering parameters of these cosmic dust analogs and hence it is not easy to rationalize the differences observed. For example, a plot of P_{max} versus steepness (or versus Q-space slope) including our results and the parameters reported by Volten et al. (2007) shows a positive slope, which is not consistent with a simple interpretation of these samples where higher porosity implies lower Q-space slope and higher P_{max}.

5.4. Scattering Properties of the Mixed Samples

Mixing of HAC and forsterite particles (50wt%) makes the phase function lower at the side and backscattering and the DLP curve lower and asymmetrical. In fact, the scattering behavior of the mixed sample is similar to that of the pure forsterite sample. The forsterite particles, which are embedded in the HAC aggregates, are much larger than the HAC monomers (Figure 7), which results in a reduction of P_{max} with respect to the HAC curve, as expected. Also, the forsterite particles reduce the porosity of the aggregates, which is also consistent with a reduction of P_{max} (Deb Roy et al. 2017). A set of similar analogs was produced by Hadamcik et al. (2020) to simulate the polarization behavior of the Zodiacal Cloud as a function of heliocentric distance, but using CB instead of HAC. The peak DLP at $\theta \sim 90°$ decreases from $P_{max} = 44\%$ for pure BC with monomer size 95 nm (Hadamcik et al. 2006) to $P_{max} = 37\%$ for a 60wt% BC mixture with minerals (of which 65wt% are compact particles) and to $P_{max} = 30\%$ for a 40wt% BC mixture, while the pure inorganic sample produced $P_{max} = 22\%$, slightly higher than the forsterite sample in Figure 8(b). In this case, the differences between the DLP of the mixtures with respect to those of the pure carbonaceous and inorganic samples are more gradual (the P_{max} of the mixtures is midway between the values for the pure BC and the mineral sample). This was probably related to the presence of porous aggregates in the mineral sample (35wt%.) and the higher absorption of CB compared to HAC.

5.5. Implications for Astronomical Observations of Circumstellar Dust

The HAC aggregates studied in this work are likely larger than the aggregates in the circumstellar shells of evolved stars, but the DLP of very porous aggregate particles at the side and backscattering angles are mainly determined by the porosity and the size of the monomers when the monomer size parameter x is equal or larger than 1 (Tazaki & Dominik 2022). Table 4 summarizes a set of observations of polarized intensity, infrared emission, and SED in the envelopes of evolved

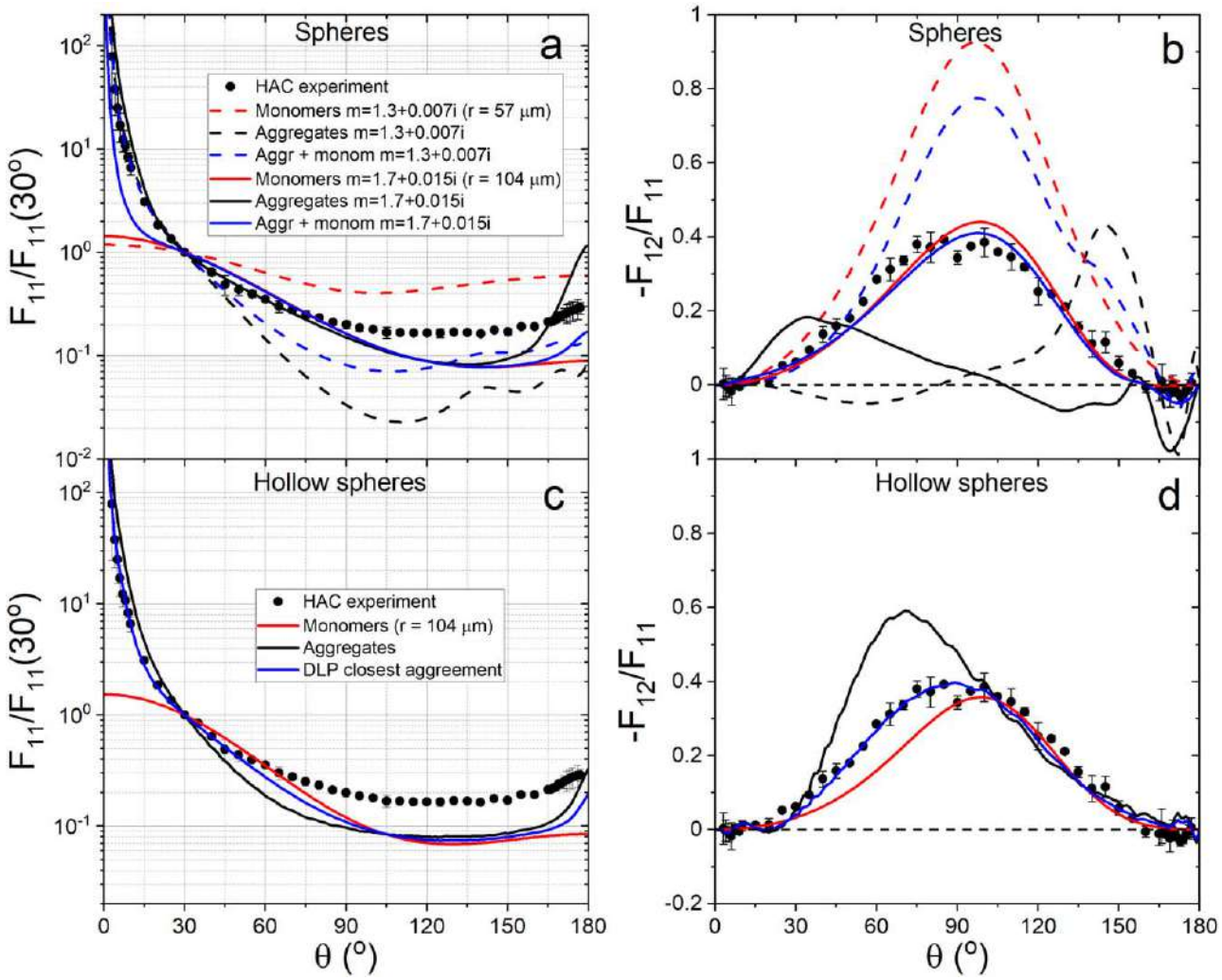

Figure 9. Top panels: simulations of the $F_{11}(\theta)/F_{11}(30^\circ)$ (panel (a)) and DLP(θ) (panel (b)) curves of the HAC sample using the spherical model. The black curves are obtained with the PSD truncated at 0.4 μm (Figure 7, filled red circles). The red curves correspond to volume log-normal distributions of spheres. The blue curves correspond to particle distributions containing both the small particles and the aggregates. Dashed lines: calculations for the effective refractive index $m = 1.3+0.007i$ and average radius of monomers $r = 57$ nm. Solid lines: calculations using the refractive index $m = 1.3+0.007i$ and adjusting the monomer size distribution to obtain reasonable agreement between the modeled and measured DLP (average radius of monomers $r = 104$ nm.). Bottom panel: simulations of the $F_{11}(\theta)/F_{11}(30^\circ)$ (panel (c)) and DLP(θ) (panel (d)) curves of the HAC sample using the DHS model. The different colored lines correspond to the same cases as above. The best fit is obtained for a maximum hollow core volume fraction of 80%.

carbon-rich stars, together with dust properties used to interpret those observations. González Delgado et al. (2003) reported light scattering by dust shells around R Sculptoris and U Antliae, with a peak DLP of 40%–50% at $\lambda \sim 589$ nm at the maximum of the dust shell (scattering angle near 90°). The observed azimuthally averaged radial profiles of scattered intensity, polarized intensity, and DLP were modeled by González Delgado et al. (2003) using a power-law distribution of spherical dust particles of amC composition. A very steep power law was required to model the observations (exponent −5.5), where the maximum contribution to scattering would originate from grains in the size range of 0.1–0.2 μm. Our analysis of the scattering pattern of HAC aggregate particles suggests that a size distribution dominated by small spherical particles can be a signature of particle monomers embedded in larger aggregate particles. The presence of micron-sized aggregates can be ascertained by measuring the phase function near forward scattering. In fact, González Delgado et al. (2003) argued that large particles would cause scattered intensities higher than actually observed along lines of sight close to the star, as an effect of enhanced forward scattering. This is an important argument (compare the phase functions of monomers and aggregates in Figure 9(a)), but we note that coronagraphic measurements are challenging and the intensity becomes more uncertain as the line of sight approaches the star (Maercker et al. 2014). This can be seen for example in the case of S Sculptoris by comparing the radial profiles of total scattered intensity reported by González Delgado et al. (2003) and Maercker et al. (2014), where the latter would admit a significantly less steep power-law size distribution, which could accommodate a population of aggregates.

6. Summary and Conclusions

A circumstellar dust analog with HAC composition has been synthesized using plasma deposition in an RF discharge. The particles formed are porous aggregates of quasi-spherical monomers with $r \sim 50$–60 nm, which resemble model particles computed by cluster-cluster and particle-cluster aggregation methods. The phase function and DLP of light scattered by a

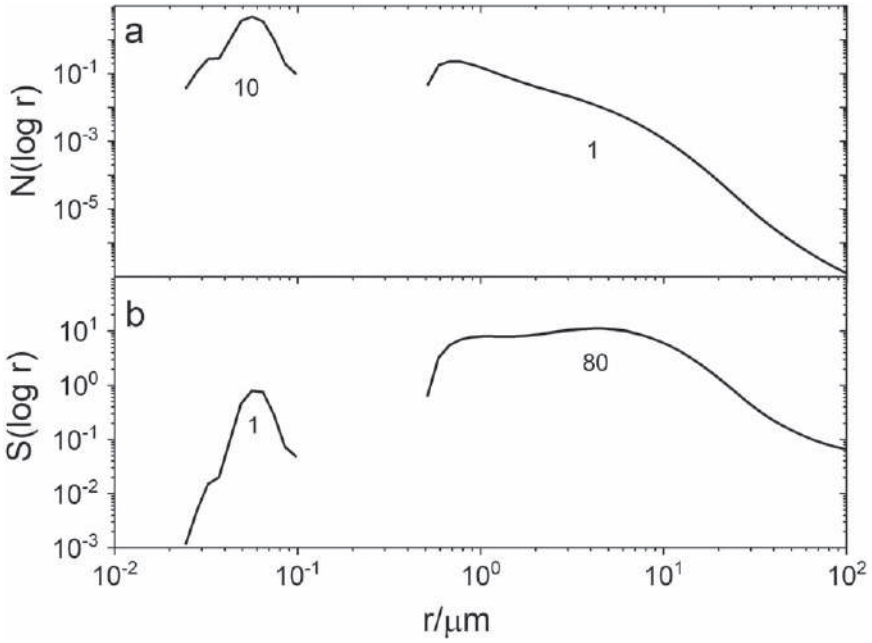

Figure 10. (a) Composite $N(\log r)$ of loose HAC monomers and aggregates assuming that they are in a 10:1 ratio as suggested by the SEM image in Figure 3(c). (b) Logarithmic-scale normalized projected surface PSD $S(\log r)$ corresponding to the number PSD in panel (b). The numbers under the curves indicate the relative contribution to the number of particles and surface for $r < 0.4$ μm and $r > 0.4$ μm.

cloud of randomly oriented particles of the sample have been measured at 514 nm for scattering angles between 3° and 177°. The scattering curves show the characteristic features of porous aggregates, including a symmetrical bell-shaped DLP, which is determined by light scattering by the monomers, whose size is comparable to the wavelength employed in the experiments ($x \sim 1$). The performance of the spherical model in modeling the scattering pattern of porous aggregates has been tested, with the following results:

1. The measured ($\lambda = 514$ nm) phase function and DLP of a (equivalent) size distribution of aggregate porous particles with an average radius $r \sim 1$ μm cannot be modeled simultaneously by a size distribution of spherical particles. The phase function is too shallow at the side scattering angles and the DLP is bell-shaped.
2. If nevertheless a spherical model is used, the size distribution of spheres required to match the measurements must contain a mode of small particles, which is not consistent with the SEM images of the samples. This mode contains too many particles and they are also larger than the actual size of the monomers.
   (a) The calculated phase function of light scattered by a collection of spherical particles with an average radius of $r \leqslant 100$ nm is shallow at the side scattering and flat in forward scattering. Combined with a phase function of micron-sized spheres (large intensity in forward scattering), it results in a modeled phase function closer to the measured phase function, i.e., a forward peak and a shallow side scattering region.
   (b) The calculated polarization induced by a collection of spherical particles with an average radius of $r \leqslant 100$ nm is bell-shaped, i.e., it is qualitatively similar to the measured polarization of the light scattered by porous aggregate particles with an average radius of $r \sim 1$ μm composed of quasi-spherical grains with average radius $r < 100$ nm. However, to match the measured polarization values quantitatively, the size of the small particles in the model must be larger than that of the real monomers. The agreement improves if the refractive index employed in the model is closer to the refractive index of the material (i.e., not an effective one).

From these results, we come to the following conclusions:

1. Fitting measured data with simplified geometries may lead to spurious results in terms of size distribution (or optical constants):
   (a) The bimodal size distribution obtained for our porous HAC aggregates through Mie theory or hollow sphere models arises from two length scales within each aggregate: the overall aggregate size and the sizes of its constituent monomers.
   (b) There are conditions where aggregates behave like an ensemble of spherical monomers (RGD). When RGD conditions are not met but the aggregates are porous, the DLP curve may still be bell-shaped as that of the separated monomers, but it has a lower maximum caused by depolarization within the aggregate. This is empirically fitted by the spherical model by increasing the monomer size.
2. The retrieval of particle properties from astronomical observations may be confounded by assumptions about particle geometry:
   (a) Spherical particles show bell-shaped DLP curves only for $r < 0.4$ μm, while irregular dust particles generally show bell-shaped DLP curves in any size range, implying that the spherical model may underestimate size systematically if the only observable available is DLP at the side scattering.
   (b) Simultaneous measurements of scattered intensity sensitive to near forward scattering angles are needed to better constrain the presence of micron-sized aggregates.

Table 4
Selected Observations of Polarized Intensity, Infrared Emission, and SED in the Dusty Envelopes of Evolved Carbon-rich Stars

Star	Observations	Model	Size	Material	Optical Constants	Reference
R Sculptoris	Imaging polarimetry	Spheres	Power law $a = -5.5$	amC	m(589 nm) = 2.28 + i0.2 (Rouleau & Martin 1991)	(González Delgado et al. 2003)
	Max DLP (589.0 ± 5 nm) = 40%		0.05 μm $\leqslant r \leqslant$ 2.5 μm			
	Max DLP (769.9 ± 5 nm) = 30%					
	Imaging polarimetry	Spheres	Single size: 0.1 μm	amC	m(589 nm) = 1.8 + i0.3 (Suh 2000)	(Maercker et al. 2014)
	Max DLP (V band) = 55%					
	Max DLP (R band) = 60%					
	Infrared emission	Spheres	Power law a = -3.5	Mixture:	amC: m(589 nm) = 2.12+i0.78 (Zubko et al. 1996)	(Hankins et al. 2018)
	Polarized intensity of Maercker et al. (2014)		0.005 μm $\leqslant r \leqslant$ 0.25 μm	amC (86%)		
				SiC (10%)		
				MgS (4%)		
	SED (far-infrared and submillimeter)	Spheres	Single size: 0.1 μm	amC	amC (Rouleau & Martin 1991; Preibisch et al. 1993; Zubko et al. 1996; Jager et al. 1998; Suh 2000)	(Brunner et al. 2018)
			Two sizes: 0.1 μm and 0.25, 0.5, 0.75, 1, 2, or 5 μm	MgS		
				SiC		
		DHS	Single grain size	amC	m(589 nm) = 1.8 + i0.3 (Suh 2000)	
		BA	Single grain size	amC	m(589 nm) = 1.8 + i0.3 (Suh 2000)	
U Antliae	Imaging polarimetry	Spheres	Power law $a = -5.5$	amC	m(589 nm) = 2.28 + i0.2 (Rouleau & Martin 1991)	(González Delgado et al. 2003)
	Max DLP (589.0 ± 5 nm) = 48%		0.05 μm $\leqslant r \leqslant$ 2.5 μm			
	Max DLP (769.9 ± 5 nm) = 50%					
	Imaging polarimetry	Spheres	Single size: 0.1 μm	amC	m(589 nm) = 1.8 + i0.3 (Suh 2000)	(Maercker et al. 2010)
	Max DLP (548.2 ± 5 nm) = 26%					
	Max DLP (589.4 ± 5 nm) = 24%					
	Max DLP (657.7 ± 5 nm) = 33%					
V644 Scorpii	Imaging polarimetry	Spheres	Single size: 0.1 μm	amC	m(589 nm) = 1.8 + i0.3 (Suh 2000)	(Maercker et al. 2014)
	Max DLP (V band) >7%					
	Max DLP (R band) >7%					
HD 56126	Infrared emission	Spheres	Power law $a = -3.5$ 0.01 μm $\leqslant r \leqslant$ 1 μm	amC, HAC, MgS, TiC	amC (Preibisch et al. 1993) HAC parameterization (Hony et al. 2003)	(Hony et al. 2003)

In particular, the analysis of polarimetric and spectroscopic astronomical observations of the dusty environments of AGB and post-AGB stars using spherical particle geometry converge in particle size estimates of $\sim 0.1\,\mu$m. However, the assumption of spherical geometry may result in an overall underestimation of particle size, or at least in missing a population of larger porous aggregates present among the population of loose individual grains. The consequence of simplified particle geometries are being explored in the context of cometary environments and protoplanetary disks, but have been less explored in the interpretation of circumstellar environments. Because of the thorough characterization of the samples, the experimental scattering data presented in this work provide an excellent benchmark for modeling light scattering using computational aggregation procedures combined with T-matrix calculations. The data is freely available for download at the Granada–Amsterdam scattering database.[6] Future experiments with circumstellar dust analogs need to address the production of different grades of hydrogenated amorphous carbon and mixtures of materials with controlled size distributions.

Acknowledgments

J.C.G.M. and O.M. acknowledge financial support from the Severo Ochoa grant CEX2021-001131-S funded by MCIN/AEI/10.13039/501100011033, the grant PID2021-123370OB-I00 (CATS) funded by MCIN/AEI/10.13039/501100011033, and the European Union NextGenerationEU/PTR. I.T., R.J.P., B.M., M.J.R., and V.J.H. acknowledge financial support by MCIN/AEI/10.13039/501100011033 under grant PID2020-113084GB-I00, by the CSIC i-Link project LINKA 20353 and by the European Research Council under grant ERC-2013-Syg-210656-NANOCOSMOS.

ORCID iDs

Juan Carlos Gómez Martín https://orcid.org/0000-0001-7972-085X
Olga Muñoz https://orcid.org/0000-0002-5138-3932
Julia Martikainen https://orcid.org/0000-0003-2211-4001
Daniel Guirado https://orcid.org/0000-0002-9228-1035
Isabel Tanarro https://orcid.org/0000-0002-1888-513X
Ramón J. Peláez https://orcid.org/0000-0002-8982-2224
Belén Maté https://orcid.org/0000-0002-5478-8644
Miguel Jiménez-Redondo https://orcid.org/0000-0001-9221-8426
Víctor J. Herrero https://orcid.org/0000-0002-7456-4832
Marco Peiteado https://orcid.org/0000-0003-3510-6676
Teresa Jardiel https://orcid.org/0000-0002-0163-7324

References

Adam, C., & Ohnaka, K. 2019, A&A, 628, A132
Arriaga, P., Fitzgerald, M. P., Duchêne, G., et al. 2020, AJ, 160, 79
Bertini, I., Gutierrez, P. J., & Sabolo, W. 2009, A&A, 504, 625
Bladh, S., Eriksson, K., Marigo, P., Liljegren, S., & Aringer, B. 2019, A&A, 623, A119
Brunner, M., Maercker, M., Mecina, M., Khouri, T., & Kerschbaum, F. 2018, A&A, 614, A17
Cannon, E., Montargès, M., de Koter, A., et al. 2021, MNRAS, 502, 369
Compagnini, G., Zammit, U., Madhusoodanan, K. N., & Foti, G. 1995, PhRvB, 51, 11168
Deb Roy, P., Halder, P., & Das, H. S. 2017, Ap&SS, 362, 209
Demyk, K. 2011, EPJWC, 18, 03001
Dischler, B., Bubenzer, A., & Koidl, P. 1983, ApPhL, 42, 636
Draine, B. T. 2003, ARA&A, 41, 241
Duley, W. W. 1985, MNRAS, 215, 259
Fonfria, J. P., Cernicharo, J., Richter, M. J., & Lacy, J. H. 2008, ApJ, 673, 445
Ghahari, M., & Naeimi, A. R. 2017, J. Rare Earths, 35, 1171
Gledhill, T. M. 2005, MNRAS, 356, 883
Godard, M., & Dartois, E. 2010, A&A, 519, A39
Gómez Martín, J. C., Guirado, D., Zubko, E., et al. 2020, JQSRT, 241, 106745
González Delgado, D., Olofsson, H., Schwarz, H. E., et al. 2003, A&A, 399, 1021
Gustafson, B. Å. S., & Kolokolova, L. 1999, JGR, 104, 31711
Güttler, C., Mannel, T., Rotundi, A., et al. 2019, A&A, 630, A24
Hadamcik, E., Lasue, J., Levasseur-Regourd, A. C., & Renard, J. 2020, P&SS, 183, 104527
Hadamcik, E., Renard, J. B., Levasseur-Regourd, A. C., & Lasue, J. 2006, JQSRT, 100, 143
Hadamcik, E., Renard, J. B., Rietmeijer, F. J. M., et al. 2007, Icar, 190, 660
Hadamcik, E., Renard, J. B., Worms, J. C., Levasseur-Regourd, A. C., & Masson, M. 2002, Icar, 155, 497
Hankins, M. J., Herter, T. L., Maercker, M., Lau, R. M., & Sloan, G. C. 2018, ApJ, 852, 27
Hansen, J. E., & Travis, L. D. 1974, SSRv, 16, 527
Henning, T., Il'in, V. B., Krivova, N. A., Michel, B., & Voshchinnikov, N. V. 1999, A&AS, 136, 405
Herrero, V. J., Jiménez-Redondo, M., Peláez, R. J., Maté, B., & Tanarro, I. 2022, FrASS, 9, 406
Hony, S., Tielens, A. G. G. M., Waters, L. B. F. M., & De Koter, A. 2003, A&A, 402, 211
Jacob, W. 1998, TSF, 326, 1
Jager, C., Mutschke, H., & Henning, T. 1998, A&A, 332, 291
Jaglarz, J., Dyndał, K., & Tkacz-Śmiech, K. 2020, J. Mater. Res. Technol., 9, 1698
Jiménez-Redondo, M., Tanarro, I., & Herrero, V. J. 2022, PSST, 31, 065003
Jiménez-Redondo, M., Tanarro, I., Peláez, R. J., Díaz-Pérez, L., & Herrero, V. J. 2019, JPCA, 123, 8135
Jones, A. P., Fanciullo, L., Köhler, M., et al. 2013, A&A, 558, A62
Kassavetis, S., Patsalas, P., Logothetidis, S., Robertson, J., & Kennou, S. 2007, DRM, 16, 1813
Khouri, T., Vlemmings, W. H. T., Olofsson, H., et al. 2018, A&A, 620, A75
Khouri, T., Vlemmings, W. H. T., Paladini, C., et al. 2020, A&A, 635, A200
Khouri, T., Waters, L. B. F. M., De Koter, A., et al. 2015, A&A, 577, A114
Kiselev, N., Rosenbush, V., Levasseur-Regourd, A.-C., & Kolokolova, L. 2015, in Polarimetry of Stars and Planetary, ed. L. Kolokolova, J. Hough, & A.-C. Levasseur-Regourd (Cambridge: Cambridge Univ. Press), 379
Kovačević, E., Stefanović, I., Berndt, J., Pendleton, Y. J., & Winter, J. 2005, ApJ, 623, 242
Lau, R. M., Hankins, M. J., Han, Y., et al. 2022, NatAs, 6, 1308
Maercker, M., Olofsson, H., Eriksson, K., Gustafsson, B., & Schöier, F. L. 2010, A&A, 511, A37
Maercker, M., Ramstedt, S., Leal-Ferreira, M. L., Olofsson, G., & Floren, H. G. 2014, A&A, 570, A110
Maté, B., Jimenez-Redondo, M., Peláez, R. J., Tanarro, I., & Herrero, V. J. 2019, MNRAS, 490, 2936
Maté, B., Molpeceres, G., Jiménez-Redondo, M., Tanarro, I., & Herrero, V. J. 2016, ApJ, 831, 51
Min, M., Hovenier, J. W., & de Koter, A. 2005, A&A, 432, 909
Min, M., Jeffers, S. V., Canovas, H., et al. 2013, A&A, 554, A15
Min, M., Rab, C., Woitke, P., Dominik, C., & Ménard, F. 2016, A&A, 585, A13
Mishchenko, M., Travis, L. D. L., & Lacis, A. A. 2002, Scattering, Absorption, and Emission of Light by Small Particles (Cambridge: Cambridge Univ. Press)
Mishchenko, M. I. 2009, JQSRT, 110, 808
Molpeceres, G., Timón, V., Jiménez-Redondo, M., et al. 2017, PCCP, 19, 1352
Muñoz, O., Frattin, E., Jardiel, T., et al. 2021, ApJS, 256, 17
Muñoz, O., Moreno, F., Guirado, D., et al. 2010, JQSRT, 111, 187
Muñoz, O., Moreno, F., Guirado, D., et al. 2011, Icar, 211, 894
Muñoz, O., Moreno, F., Guirado, D., et al. 2012, JQSRT, 113, 565
Nuth, J. a., Hallenbeck, S. L., & Rietmeijer, F. J. M. 2000, JGR, 105, 10387
O'Donnell, J. E. 1994, ApJ, 437, 262
Ohnaka, K., Weigelt, G., & Hofmann, K. H. 2016, A&A, 589, A91
Olofsson, H., Maercker, M., Eriksson, K., Gustafsson, B., & Schöier, F. 2010, A&A, 515, A27
Peláez, R. J., Maté, B., Tanarro, I., et al. 2018, PSST, 27, 035007
Pendleton, Y. J., & Allamandola, L. J. 2002, ApJS, 138, 75

[6] http://scattering.iaa.csic.es/

Preibisch, Th., Ossenkopf, V., Yorke, H. W., et al. 1993, A&A, 279, 577
Ramstedt, S., Maercker, M., Olofsson, G., Olofsson, H., & Schöier, F. L. 2011, A&A, 531, A148
Rietmeijer, F. J. M., & Karner, J. M. 1999, JChPh, 110, 4554
Rouleau, F., & Martin, P. G 1991, ApJ, 377, 526
Santoro, G., Martínez, L., Lauwaet, K., et al. 2020, ApJ, 895, 97
Smith, F. W. 1984, JAP, 55, 764
Sorensen, C., Heinson, Y., Heinson, W., Maughan, J., & Chakrabarti, A. 2017, Atmos, 8, 68
Sorensen, C. M. 2001, AerST, 35, 648
Suh, K.-W. 2000, MNRAS, 315, 740
Tazaki, R., & Dominik, C. 2022, A&A, 663, A57
Tazaki, R., Tanaka, H., Okuzumi, S., Kataoka, A., & Nomura, H. 2016, ApJ, 823, 70
Toon, O. B., & Ackerman, T. P. 1981, ApOpt, 20, 3657
Volten, H., Muñoz, O., Hovenier, J. W., et al. 2007, A&A, 470, 377
Voshchinnikov, N. V., Il'in, V. B., & Henning, T. 2005, A&A, 429, 371
Voshchinnikov, N. V., Videen, G., & Henning, T. 2007, ApOpt, 46, 4065
Zeinert, A., Arnas, C., Dominique, C., & Mouberi, A. 2008, JVSTA, 26, 1450
Zerda, T. W., Xu, W., Yang, H., & Gerspacher, M. 1998, Rubber Chem. Technol., 71, 26
Zhukovska, S., Henning, T., & Dobbs, C. 2018, ApJ, 857, 94
Zubko, V. G., Mennella, V., Colangeli, L., & Bussoletti, E. 1996, MNRAS, 282, 1321

The Astrophysical Journal Supplement Series, 271:65 (1pp), 2024 April https://doi.org/10.3847/1538-4365/ad3335

Erratum: "Experimental Phase Function and Degree of Linear Polarization of Light Scattered by Hydrogenated Amorphous Carbon Circumstellar Dust Analogs" (2023, ApJS, 270, 2)

Juan Carlos Gómez Martín[1], Olga Muñoz[1], Julia Martikainen[1], Daniel Guirado[1], Isabel Tanarro[2], Ramón J. Peláez[2], Belén Maté[2], Miguel Jiménez-Redondo[2,4], Víctor J. Herrero[2], Marco Peiteado[3], and Teresa Jardiel[3]
[1] Instituto de Astrofísica de Andalucía (IAA-CSIC), Glorieta de la Astronomía s/n, 18008 Granada, Spain; jcgomez@iaa.es, olga@iaa.es
[2] Instituto de Estructura de la Materia (IEM-CSIC), Serrano 121-123, 28006 Madrid, Spain
[3] Instituto de Cerámica y Vidrio (ICV-CSIC), Kelsen 5, Campus Cantoblanco, 28049 Madrid, Spain
Received 2024 March 11; published 2024 April 12

In the caption of Figure 2, the spectral curves of HAC and HAC + forsterite are mislabeled. Instead of stating "Imaginary part of the refractive index of HAC (red line) and HAC + forsterite (black line)," it should read "Imaginary part of the refractive index of HAC (black line) and HAC + forsterite (red line)."

ORCID iDs

Juan Carlos Gómez Martín https://orcid.org/0000-0001-7972-085X
Olga Muñoz https://orcid.org/0000-0002-5138-3932
Julia Martikainen https://orcid.org/0000-0003-2211-4001
Daniel Guirado https://orcid.org/0000-0002-9228-1035
Isabel Tanarro https://orcid.org/0000-0002-1888-513X
Ramón J. Peláez https://orcid.org/0000-0002-8982-2224
Belén Maté https://orcid.org/0000-0002-5478-8644
Miguel Jiménez-Redondo https://orcid.org/0000-0001-9221-8426
Víctor J. Herrero https://orcid.org/0000-0002-7456-4832
Teresa Jardiel https://orcid.org/0000-0002-0163-7324

[4] Present address: Max-Planck-Institute for Extraterrestrial Physics, Gießenbachstraße 1, 85748, Garching, Germany.